







Magnetic domain wall curvature induced by wire edge pinning

Cite as: Appl. Phys. Lett. **117**, 062406 (2020); <https://doi.org/10.1063/5.0010798>

Submitted: 14 April 2020 . Accepted: 06 July 2020 . Published Online: 14 August 2020

L. Herrera Diez , F. Ummelen, V. Jeudy, G. Durin, L. Lopez-Diaz , R. Diaz-Pardo, A. Casiraghi , G. Agnus, D. Bouville, J. Langer , B. Ocker , R. Lavrijsen , H. J. M. Swagten, and D. Ravelosona



View Online



Export Citation



CrossMark

ARTICLES YOU MAY BE INTERESTED IN

[Quantum size effect in nanocorrals: From fundamental to potential applications](#)

Applied Physics Letters **117**, 060501 (2020); <https://doi.org/10.1063/5.0015542>

[Dynamically reconfigurable magnonic crystal composed of artificial magnetic skyrmion lattice](#)

Journal of Applied Physics **128**, 063901 (2020); <https://doi.org/10.1063/5.0012791>

[Spin wave generation via localized spin-orbit torque in an antiferromagnet-topological insulator heterostructure](#)

Journal of Applied Physics **128**, 043901 (2020); <https://doi.org/10.1063/5.0010478>

 Measure Ready
FastHall™ Station

The highest performance tabletop system
for van der Pauw and Hall bar samples



Learn more

 Lake Shore
CRYOTRONICS

AIP
Publishing

Magnetic domain wall curvature induced by wire edge pinning

Cite as: Appl. Phys. Lett. **117**, 062406 (2020); doi: 10.1063/5.0010798

Submitted: 14 April 2020 · Accepted: 6 July 2020 ·

Published Online: 14 August 2020



View Online



Export Citation



CrossMark

L. Herrera Diez,^{1,a)}  F. Ummelen,² V. Jeudy,³ G. Durin,⁴ L. Lopez-Diaz,⁵  R. Diaz-Pardo,³ A. Casiraghi,⁴ 
G. Agnus,¹ D. Bouville,¹ J. Langer,⁶  B. Ocker,⁶  R. Lavrijsen,²  H. J. M. Swagten,² and D. Ravelosona¹

AFFILIATIONS

¹Centre de Nanosciences et de Nanotechnologies, CNRS, Université Paris-Saclay, 91120 Palaiseau, France

²Department of Applied Physics, Eindhoven University of Technology, 5600 MB Eindhoven, The Netherlands

³Laboratoire de Physique des Solides, CNRS, Université Paris-Saclay, 91405 Orsay Cedex, France

⁴Istituto Nazionale di Ricerca Metrologica, Strada delle Cacce 91, 10135 Torino, Italy

⁵Departamento de Física Aplicada, Universidad de Salamanca, Plaza de la Merced s/n., 37008 Salamanca, Spain

⁶Singulus Technology AG, Hanauer Landstrasse 103, 63796 Kahl am Main, Germany

^{a)} Author to whom correspondence should be addressed: liza.herrera-diez@c2n.upsaclay.fr

ABSTRACT

In this study, we report on the analysis of the magnetic domain wall (DW) curvature due to magnetic field induced motion in Ta/CoFeB/MgO and Pt/Co/Pt wires with perpendicular magnetic anisotropy. In wires of 20 μm and 25 μm , a large edge pinning potential produces the anchoring of the DW ends to the wire edges, which is evidenced as a significant curvature of the DW front as it propagates. As the driving magnetic field is increased, the curvature reduces as a result of the system moving away from the creep regime of DW motion, which implies a weaker dependence of the DW dynamics on the interaction between the DW and the wire edge defects. A simple model is derived to describe the dependence of the DW curvature on the driving magnetic field and allows us to extract the parameter σ_E , which accounts for the strength of the edge pinning potential. The model describes well the systems with both weak and strong bulk pinning potentials like Ta/CoFeB/MgO and Pt/Co/Pt, respectively. This provides a means to quantify the effect of edge pinning induced DW curvature on magnetic DW dynamics.

Published under license by AIP Publishing. <https://doi.org/10.1063/5.0010798>

Understanding the behavior of magnetic domain walls (DWs) when transitioning from full films into patterned structures is of great importance for developing nanodevices for DW based technologies.¹ The analysis of DW dynamics in the so-called creep regime of motion,^{2–5} where defects play a central role, is a key aspect. In Ta/CoFeB/MgO/Ta films with perpendicular anisotropy bulk defect densities, and therefore depinning fields (H_{dep}), are relatively low.^{6–8} In Pt/Co/Pt films, for example, the values of H_{dep} can be more than one order of magnitude higher.^{2,4,5} Due to this low bulk pinning potential, the DW dynamics can be easily controlled even in full films by artificial pinning imposed through homogeneous material engineering processes, like light ion irradiation^{9–11} or pre-patterned substrates.¹²

Defects generated through micro/nanostructuring can also have a great impact on pristine materials. DW velocities even in micrometer size wires have been found to experience a critical decrease below the creep law dependence at low drive, which scales with the wire width.¹³

This effect is also accompanied by an increase in the curvature of the DW front and has, therefore, been attributed to edge pinning. A deeper analysis of the DW curvature in wires is, therefore, needed in view of miniaturization for technological applications.

In this study, we present the analysis of the DW curvature in a series of 20 μm wide Ta/CoFeB/MgO/Ta wires as a function of the magnetic field. The large edge pinning potential defines curvatures that at low drive reach the maximum radius $R = w/2$, where w is the wire width. We present a simple model that accounts for the variations in the DW curvature as a function of the driving magnetic field allowing for the extraction of σ_E , a parameter that characterizes the strength of the edge pinning potential. We also apply the same analysis to Pt/Co/Pt 25 μm wide wires, which present a higher intrinsic bulk pinning potential. The model describes well both systems, which shows that it can be used to assess the strength of edge pinning and its influence on DW dynamics for different bulk pinning potentials.

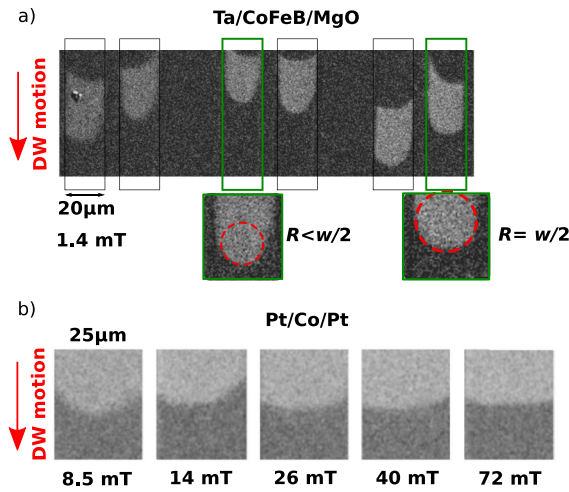


FIG. 1. (a) Kerr microscopy images of curved DWs in CoFeB wires. (b) DW curvature in a Pt/Co/Pt wire as a function of the magnetic field.

The samples investigated are Si/SiO₂/Ta (5 nm)/Co₂₀Fe₆₀B₂₀ (1 nm)/MgO (2 nm)/Ta (3 nm) films deposited by magnetron sputtering and annealed at 300 °C, exhibiting perpendicular magnetic anisotropy. A series of 20 μm wires was fabricated by photolithography and ion beam etching. The 25 μm wide Pt/Co/Pt wires were fabricated by depositing a stack of Ta (4 nm)/Pt (4 nm)/Co (0.6 nm)/Pt (4 nm) by magnetron sputtering using e-beam lithography. The final wire structure was achieved by conducting a lift-off process. Table I presents the values of saturation magnetization (M_s), effective perpendicular anisotropy constant (K_{eff}), wire width, and depinning field (H_{dep}) for the two types of samples. H_{dep} corresponds to the experimentally determined transition between the creep and depinning regimes of DW motion.^{4,5,14}

Figure 1 shows the Kerr microscopy images of the DW curvature for (a) the six CoFeB wires investigated, where curved DWs propagate under a magnetic field of 1.4 mT (expanding domains have a light gray color). In Fig. 1(b), the images show the evolution of the DW curvature with the increasing magnetic field in a Pt/Co/Pt wire, where as the driving field increases, the DW curvature is progressively suppressed. The difference in the applied fields at which large curvatures are observed for each film scales with the values of H_{dep} . This shows that the DW curvature is closely linked to a pinning mechanism.

In order to gain more insight into this behavior, let us first consider a DW propagating in a strip as shown in Fig. 2(a). In this scenario, the propagating DW remains straight and the Zeeman energy gain (dE_s) that the system experiences by letting the DW propagate a distance Δx is the following:

TABLE I. M_s , K_{eff} , the wire width (w), and the depinning fields H_{dep} for the Ta/CoFeB/MgO/Ta and Pt/Co/Pt wires.

Material	Width (μm)	M_s (A/m)	K_{eff} (J/m ³)	H_{dep} (mT)
CoFeB	20	8.7×10^5	3.4×10^5	9.7
Pt/Co/Pt	25	1.4×10^6	1.3×10^6	100.0

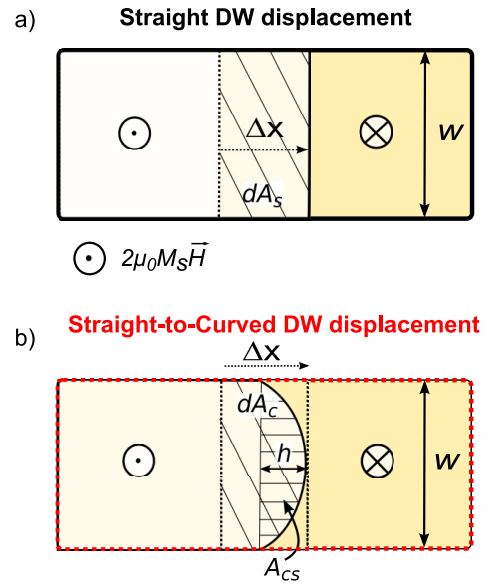


FIG. 2. Straight DW (a) and DW that transitions between a straight and a curved profile upon displacement (b).

$$dE_s = -2M_s \cdot H \cdot t \cdot dA_s, \quad (1)$$

where t is the thickness of the magnetic wire and dA_s is the area swept by the DW [see Fig. 2(a)]. Let us now consider again an initial state where the DW is straight and moves by the same amount (Δx). However, the initially straight DW front can now develop a curvature of radius R as it propagates, and this straight-to curved DW displacement is depicted in Fig. 2(b). In this case, the Zeeman energy gain is expressed as follows:

$$dE_c = \sigma \cdot t \cdot dL - 2M_s \cdot H \cdot t \cdot dA_c. \quad (2)$$

The gain in energy is reduced by the appearance of the first term that accounts for the variation in DW length dL with respect to the initial state where the DW is straight. For a straight DW, its length is equal to $L = w$, while for a curved profile, $L = 2R \arcsin(\frac{w}{2R})$. This means that the additional energy cost due to the DW curvature is linked to an increase in the DW length equal to $dL = 2R \cdot \arcsin(\frac{w}{2R}) - w$.

The energy gain for a curved wall is also further reduced due to the smaller area swept by the DW. For a straight DW, the area is $dA_s = w \cdot \Delta x$, while for the curved DW, it takes the following form:

$$dA_c = w \cdot (\Delta x - h) + A_{CS}, \quad (3)$$

where h is the sagitta as indicated in Fig. 2(b) and A_{CS} is the area of the circular sector, which can be expressed as follows:

$$h = R - \sqrt{R^2 - \frac{w^2}{4}}, \quad (4)$$

$$A_{CS} = \frac{RL}{2} - \frac{w}{2} \cdot \sqrt{R^2 - \frac{w^2}{4}}. \quad (5)$$

Using these expressions, we can now calculate dE_s and compare it to dE_c when, for example, the curvature radius is $R = 10 \mu\text{m}$ and

$w = 20 \mu\text{m}$. It is not surprising to find that if no edge pinning is involved, it is more energetically favorable for the DW to remain straight for all applied magnetic fields. Figure 3 shows the result of this calculation considering the CoFeB parameters informed in Table I; the energy gain of a straight DW (solid blue line) is always more negative than that of a curved DW (solid green line) in the whole magnetic field range.

Up to this moment, no edge pinning was considered. As it is known, the curved DW scenario [Fig. 2(b)] is a strategy to overcome edge pinning. Therefore, in order to accurately compare it to a straight DW scenario [Fig. 2(a)], this last configuration should also include an energy cost associated with keeping the DW straight in the presence of edge pinning instead of allowing a curvature to appear. In a previous study,¹³ we have proposed an additional energy term to account for deviations from the creep law that are observed due to a strong edge pinning potential in CoFeB. This term includes the parameter σ_E that can be used to quantify the strength of the edge pinning and describes the effect of the pull-back that the DW experiences in a strong edge pinning potential.

In the present case, the increase in the DW length observed in curved DWs due to edge pinning is taken into account by the term $\sigma \cdot t \cdot dL$. Let us assume that this energy cost due to edge pinning can find its counterpart in the hypothetical straight DW scenario as an increase in the DW energy equal to

$$\sigma \cdot t \cdot dL = d\sigma \cdot t \cdot w. \quad (6)$$

In this context, the difference in the DW energy between the initial and final states of the straight DW after a displacement Δx is proposed to be given by $d\sigma = 2\sigma_E$. This increment accounts for the effect of having two strong anchoring points of the DW at each wire side but no bending; therefore, the expression for dE_s takes the form

$$dE_s = 2\sigma_E \cdot t \cdot w - 2M_s \cdot H \cdot t \cdot dA_s. \quad (7)$$

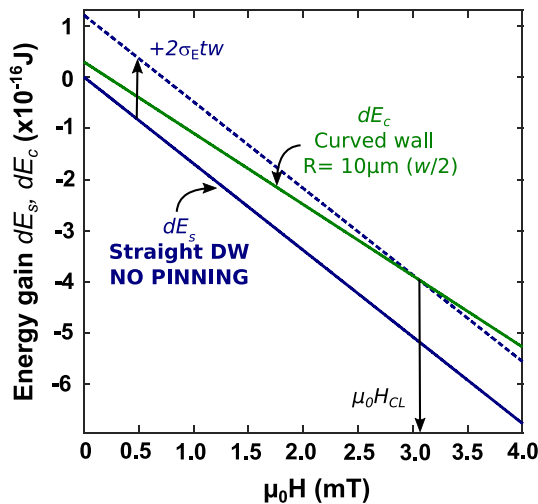


FIG. 3. Energy gain dE_s (blue line) and dE_c (green line) for straight and curved DWs as a function of the applied magnetic field in CoFeB. The straight DW without pinning increases its energy when the term $2\sigma_E \cdot t \cdot w$ is added to account for edge pinning (dotted blue line).

The addition of this term shifts dE_s toward higher energies producing a crossing with dE_c as shown in Fig. 3 (dashed blue line). This crossing is the point where $dE_s = dE_c$ and defines a field limit (H_{CL}) for the existence of a DW curvature with radius R . Above this field value, it is more energetically favorable for the DW to remain straight even in the presence of edge pinning. Reordering the terms in $dE_s = dE_c$ allows us to extract the expression for H_{CL} , which has the following form:

$$H_{CL} = \frac{\sigma_E \cdot w - \sigma \cdot dL}{2M_s \cdot (w \cdot h - A_{CS})}. \quad (8)$$

Substituting for dL , h , and A_{CS} introduces R in the equation and allows for the evaluation of the dependence of the field limit on a given range of DW curvatures ($1/R$). The experimentally observed DW curvature dependence on the applied magnetic field (symbols) together with the calculated H_{CL} (solid line) is shown in Fig. 4(a) for CoFeB and in (b) for Pt/Co/Pt. It is worth mentioning once again that this model describes the field limit under which a given curvature can be observed, which includes the possibility of one curvature appearing at different magnetic fields below H_{CL} .

The model presented here is valid up to a maximum curvature of $2/w$; however, at low drive, higher curvatures are observed for both CoFeB and Pt/Co/Pt. This occurs at magnetic fields below the value needed to depin the DW from the wire edges, even at the expense of a maximum curvature, but well above that needed to overcome pinning at the center of the wire. In this case, it may be more energetically favorable for a DW to increase its length going from the edges to the center of the wire to increase the switched area. In this context, the DW front could take a more triangular shape and exhibit at the center a curvature smaller than $w/2$. This effect can be visualized in the wires at the center of Fig. 2(a). The description of the curvatures above $2/w$ ($R < w/2$) at low drive is not considered in this model.

The solid curves representing H_{CL} provide a dividing line between curved and straight DWs in a magnetic field map. As mentioned, the calculation of these curves takes into account the values of K_{eff} , M_s , and the width of the wire, while the value of σ_E is adjusted to model the results. The values of σ_E obtained for CoFeB and Pt/Co/Pt are 1.01×10^{-2} N/m and 6.35×10^{-2} N/m, respectively. σ_E has been introduced in a previous study as a means to quantify the strength of the edge pinning potential in the context of edge-pinning induced deviations from the creep law in CoFeB wires.¹³ In this framework, it is particularly interesting to compare σ_E to the DW surface tension $\sigma = 4\sqrt{A_{ex} \cdot K_{eff}}$, where A_{ex} is the exchange stiffness constant (2.3×10^{-11} J/m for CoFeB and 1.6×10^{-11} J/m for Pt/Co/Pt). The ratio σ/σ_E results in 1.1 and 0.28 for CoFeB and Pt/Co/Pt wires, respectively. It has been proposed¹³ that as this ratio decreases, the edge pinning potential represented by σ_E progressively dominates over the DW surface energy allowing for a DW curvature. However, when comparing values for different materials, not only the differences in the intrinsic parameters but also of the bulk pinning potentials need to be taken into account. The effect of the edge pinning potential depends on its relative strength with respect to the bulk pinning potential, intimately related to the value of the depinning field H_{dep} .

The measured DW curvatures in CoFeB and Pt/Co/Pt cover a similar range going from those corresponding to $R = w/2$ down to low values corresponding to a large R (higher than $R = w/0.4$) for nearly straight DWs. However, the magnetic field range over which each curvature is observed is significantly different with respect to H_{dep} , which

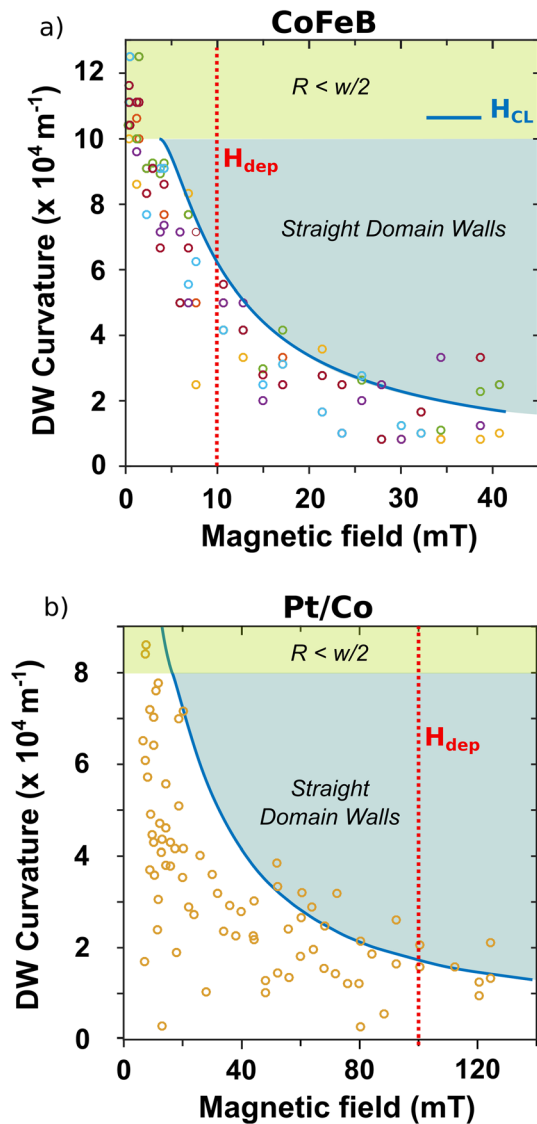


FIG. 4. Domain wall curvature as a function of magnetic field in a 20 μm wide CoFeB wire (a, different colors correspond to the different wires shown in Fig. 1) and in a 25 μm wide Pt/Co/Pt wire. The solid lines are the calculation of H_{CL} .

is marked by red lines in Figs. 4(a) and 4(b). In CoFeB at H_{dep} , the maximum DW curvature observed experimentally and also described by the model is $6 \times 10^{-4} \text{ m}^{-1}$ ($R = w/1.2$). The DW curvature is still relatively pronounced and continues to be well beyond the creep regime. Only at fields around 30 mT, three times larger than H_{dep} , do the DWs become relatively straight, showing a maximum curvature of $2 \times 10^{-4} \text{ m}^{-1}$ ($R = w/0.4$). In contrast, the Pt/Co/Pt wires at H_{dep} already show relatively straight DWs with a maximum curvature below $2 \times 10^{-4} \text{ m}^{-1}$. This can be related to the large differences of about one order of magnitude found in the depinning field for the two materials. This difference also exists in full films and is due to the intrinsic bulk pinning potential that is known to be exceptionally low in CoFeB materials.^{2,6} In this context, a relatively small edge pinning

potential can already have a large impact on the dynamics in CoFeB, while a much larger one is needed to dominate the DW dynamics in Pt/Co/Pt. Consequently, the edge pinning potential in CoFeB induces a much stronger effect than in Pt/Co/Pt, reflected here in the strong and persisting curvature of the DWs even beyond the creep regime. In contrast, in Pt/Co/Pt, a significant DW curvature induced by edge pinning is only observed deep into the creep regime.

This model can also be used to extrapolate the effects of edge pinning to narrower wires. Figure 5(a) shows the calculated H_{CL} profiles using $\sigma_E = 1.01 \times 10^{-2} \text{ N/m}$, the intrinsic parameters for CoFeB and varying the wire width. The H_{CL} values increase as the wire becomes narrower. The plot in the inset of Fig. 5(a) shows the H_{CL} values for a DW radius of $w/2$ as a function of the wire width; here, a dramatic increase is observed for narrow wires. This model could, therefore, allow for the estimation of the effects of edge pinning for a given material and a particular wire edge structure, for example, linked to the fabrication process, as the wire width decreases. The estimation could be conveniently performed by analyzing the DW dynamics at much larger scales.

For wires widths below $5 \mu\text{m}$, it is interesting to compare this analytical model with micromagnetic simulations. Figure 5(b) shows the result for CoFeB wires; filled squares and circles represent the curvatures observed for $w = 4 \mu\text{m}$ and $w = 2 \mu\text{m}$ with a maximum edge roughness (M_{ER}) of 30 nm (see the supplementary material). The DW curvature follows a similar trend to the analytical model with respect to magnetic field and w . M_{ER} plays a key role; empty squares show the trend obtained for $w = 4 \mu\text{m}$ and $M_{ER} = 80 \text{ nm}$, which is reflected in a shift of the curvatures at all magnetic fields to significantly higher values. The curvature at 40 mT was also evaluated in a wire with very rough edges, $M_{ER} = 300 \text{ nm}$, showing a further increase (crossed diamond). This is in line with the conclusions made earlier regarding the effects of the fabrication process on the DW curvature.

The curve obtained using the analytical model for $w = 4 \mu\text{m}$ is shown in Fig. 5(b); the curvatures are significantly larger than those obtained with micromagnetic simulations even for very large M_{ER} . It is, therefore, important to highlight that the micromagnetic simulations were made using the experimental values presented in Table I while exploring the effect of variations in the Gilbert damping parameter α . The curvatures for $w = 4 \mu\text{m}$ in open and full squares and the

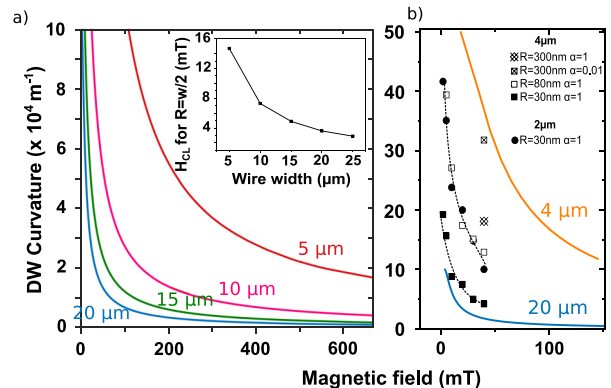


FIG. 5. (a) Calculated H_{CL} profile for $\sigma_E = 1.01 \times 10^{-2} \text{ N/m}$ (CoFeB) for different wire widths. H_{CL} values corresponding to $R = w/2$ as a function of the wire width (inset). (b) Comparison with micromagnetic simulations.

crossed diamond were calculated using $\alpha = 1$, all showing relatively low values. For high M_{ER} , changing α from 1 (crossed diamond) to 0.01 (crossed square) increases significantly the curvature, as seen at 40 mT. CoFeB is known to have low values of α in the 0.015 range;⁶ therefore, lower α values not only give curvatures closer to the analytical model but are also more compatible with experimental values.

In contrast, for low M_{ER} , the effect of varying α is not a dominant feature. This brings attention to the crucial role of disorder in the DW dynamics in CoFeB. In the present study, perfect wires are simulated, while studies in the literature show that adding a granular structure and an anisotropy distribution to simulate disorder can have a large impact on the DW dynamics. In this context, additional energy dissipation channels appear in the system, which could also affect the response to a change in the value of α .¹¹ A detailed micromagnetic study would be needed to fully characterize these effects.

Micromagnetic simulations have also been performed for $w = 250$ nm and $w = 500$ nm, where the analytical model finds its limit of validity since it is based on the one dimensional (1D) model of DW motion. A dimensionality change may occur from a 2D to a 1D medium for very narrow wires¹⁵ and edge effects can rule over creep dynamics,¹⁶ limiting the use of a 1D based model. For $w = 500$ nm, $M_{ER} = 30$ nm, and $\alpha = 0.015$, the internal structure of the DW presents a large number of Bloch lines and an irregular DW front, showing no curvature for either 10 mT or 20 mT. A similar behavior is observed for $w = 250$ nm (see the [supplementary material](#)). This confirms the presence of a more complex dynamics at this scale going beyond the 1D model and calls for a more careful theoretical analysis.

In conclusion, we present a simple model to describe the dependence of the DW curvature on the applied magnetic fields in wires with an edge pinning potential. This model allows for the estimation of the magnetic field limit up to which a given DW curvature can be observed, and it has been applied to two key spintronics materials with low and high bulk pinning potentials, CoFeB and Pt/Co/Pt. The analysis of the DW curvature also allows for the extraction of the parameter σ_E , which can be used to compare edge pinning potentials in different devices. The relative strength of the edge pinning potential with respect to the surface tension of the DW (σ/σ_E) and the differences between the edge and bulk pinning potentials in each material are the key aspects involved in the description of the DW curvature. It has also been shown that this model can be used to extrapolate the effects of edge pinning observed in relatively large wires to smaller dimensions and has a good correspondence with the results obtained from micromagnetic simulations. Therefore, this model can be of considerable interest for the understanding and quantification of the effects of edge pinning in patterned magnetic structures.

See the [supplementary material](#) for information about micromagnetic simulations.

We gratefully acknowledge financial support from the European Union FP7 and H2020 Programs (MSCA ITN Grant Nos. 608031 and 860060), the French National Research Agency (project ELECSPIN), and Ministerio de Economía y Competitividad of the Spanish Government (Project No. MAT2017-87072-C4-1-P). The authors thank G. van der Jagt for useful comments.

DATA AVAILABILITY

The data that support the findings of this study are available from the corresponding author upon reasonable request.

REFERENCES

- S. P. Parkin, M. Hayashi, and L. Thomas, *Science* **320**, 190–194 (2008).
- P. J. Metaxas, J. P. Jamet, A. Mougin, M. Cormier, J. Ferre, V. Baltz, B. Rodmacq, B. Dieny, and R. L. Stamps, *Phys. Rev. Lett.* **99**, 217208 (2007).
- P. Metaxas, *Solid State Physics* (Academic Press Inc., 2011), Vol. 62, Chap. 2.
- S. Lemerle, J. Ferré, C. Chappert, V. Mathet, T. Giamarchi, and P. Le Doussal, *Phys. Rev. Lett.* **80**, 849 (1998).
- V. Jeudy, A. Mougin, S. Bustingorry, W. Savero Torres, J. Gorchon, A. B. Kolton, A. Lemaître, and J.-P. Jamet, *Phys. Rev. Lett.* **117**, 057201 (2016).
- C. Burrows, N. Vernier, J.-P. Adam, L. Herrera Diez, K. Garcia, I. Barisic, G. Agnus, S. Eimer, J.-V. Kim, T. Devolder, A. Lamperti, R. Mantovan, B. Ockert, E. E. Fullerton, and D. Ravelosona, *Appl. Phys. Lett.* **103**, 182401 (2013).
- R. Lavrijsen, G. Malinowski, J. H. Franken, J. T. Kohlhepp, H. J. M. Swagten, B. Koopmans, M. Czapkiewicz, and T. Stobiecki, *Appl. Phys. Lett.* **96**, 022501 (2010).
- J.-P. Tetienne, T. Hingant, J.-V. Kim, L. Herrera Diez, J.-P. Adam, K. Garcia, J.-F. Roch, S. Rohart, A. Thiaville, D. Ravelosona, and V. Jacques, *Science* **344**, 1366 (2014).
- J. Fassbender, D. Ravelosona, and Y. Samson, *J. Phys. D* **37**, R179–R196 (2004).
- L. Herrera Diez, F. García-Sánchez, J.-P. Adam, T. Devolder, S. Eimer, M. S. El Hadri, A. Lamperti, R. Mantovan, B. Ocker, and D. Ravelosona, *Appl. Phys. Lett.* **107**, 032401 (2015).
- L. Herrera Diez, M. Voto, A. Casiraghi, M. Belmuguenai, Y. Roussigné, G. Durin, A. Lamperti, R. Mantovan, V. Sluka, V. Jeudy, Y. T. Liu, A. Stashkevich, S. M. Chérif, J. Langer, B. Ocker, L. Lopez-Diaz, and D. Ravelosona, *Phys. Rev. B* **99**, 054431 (2019).
- A. Digiaco, R. Mantovan, N. Vernier, T. Devolder, K. Garcia, G. Tallarida, M. Fanciulli, A. Lamperti, B. Ocker, L. Baldi, M. Mariani, and D. Ravelosona, *Phys. Rev. Appl.* **10**, 064053 (2018).
- L. Herrera Diez, V. Jeudy, G. Durin, A. Casiraghi, Y. T. Liu, M. Voto, G. Agnus, D. Bouville, L. Vila, J. Langer, B. Ocker, L. Lopez-Diaz, and D. Ravelosona, *Phys. Rev. B* **98**, 054417 (2018).
- R. D. Pardo, W. Savero Torres, A. B. Kolton, S. Bustingorry, and V. Jeudy, *Phys. Rev. B* **95**, 184434 (2017).
- K.-J. Kim, J.-C. Lee, S.-M. Ahn, K.-S. Lee, C.-W. Lee, Y. J. Cho, S. Seo, K.-H. Shin, S.-B. Choe, and H.-W. Lee, *Nature* **458**, 740 (2009).
- X. Zhang, N. Vernier, W. Zhao, L. Vila, and D. Ravelosona, *AIP Adv.* **8**, 056307 (2018).